# The Structure of the Evolved Circumbinary Disk around V4046 Sgr

Katherine A. Rosenfeld<sup>1</sup>, Sean M. Andrews<sup>1</sup>, David J. Wilner<sup>1</sup>, J. H. Kastner<sup>2</sup>, & M. K. McClure<sup>3</sup>

#### ABSTRACT

We present sensitive, sub-arcsecond resolution Submillimeter Array observations of the protoplanetary disk around the nearby, pre-main sequence spectroscopic binary V4046 Sgr. We report for the first time a large inner hole  $(r = 29 \,\mathrm{AU})$  spatially resolved in the 1.3 mm continuum emission and study the structure of this disk using radiative transfer calculations to model the spectral energy distribution (SED), continuum visibilities, and spectral line emission of CO and its main isotopologues. Our modeling scheme demonstrates that the majority of the dust mass is distributed in a narrow ring (centered at 37 AU with a FWHM of 16 AU) that is  $\sim 5 \times$  more compact than the gas disk. This structure implies that the dust-to-gas mass ratio has a strong spatial variation, ranging from a value much larger than typical of the interstellar medium (ISM) at the ring to much smaller than that of the ISM at larger disk radii. We suggest that these basic structural features are potentially observational signatures of the accumulation of solids at a local gas pressure maximum. These models also require a substantial population of  $\sim \mu$ m-sized grains inside the central disk cavity. We suggest that this structure is likely the result of dynamical interactions with a low-mass companion, although photoevaporation may also play a secondary role.

Subject headings: circumstellar matter — protoplanetary disks — planet-disk interactions — submillimeter: planetary systems — stars: individual (V4046 Sgr)

#### 1. Introduction

In the past few years, high angular resolution millimeter/radio-wave observations have facilitated rapid development in our understanding of some fundamental aspects of protoplanetary disk evolution. For example, there is mounting evidence for substantial discrepancies between the spatial distributions of mm-sized dust particles and molecular gas in protoplanetary disks, possibly caused by a dramatic decrease in the dust-to-gas ratio at large radii (e.g., Panić et al. 2009; Andrews et al. 2012). Coupling those results with new analyses that identify a systematic decrease in dust particle sizes in the outer disk (Guilloteau et al. 2011; Pérez et al. 2012), there seems to be good progress

<sup>&</sup>lt;sup>1</sup>Harvard-Smithsonian Center for Astrophysics, 60 Garden Street, Cambridge, MA 02138

<sup>&</sup>lt;sup>2</sup>Center for Imaging Science, Rochester Institute of Technology, 54 Lomb Memorial Drive, Rochester, NY 14623

<sup>&</sup>lt;sup>3</sup>Department of Astronomy, University of Michigan, 830 Dennison Bldg, 500 Church Street, Ann Arbor, MI 48109

toward the promise of empirical constraints on the key processes tied to the growth and migration of disk solids. Meanwhile, there has been marked improvement in the characterization of another key factor in disk evolution: dynamical interactions with companions. Harris et al. (2012) provided a sweeping quantitative confirmation of the seminal work by Jensen et al. (1996), demonstrating that tidal interactions in multiple star systems are a prominent issue for disk survival, especially for separations in the  $\sim 3-30\,\mathrm{AU}$  range. And Andrews et al. (2011a) (among others) have speculated that the ring-like millimeter-wave dust continuum emission morphologies noted for the so-called "transition" disks are most likely created by an analogous dynamical interaction process, though in this case the perturbers may be embedded planetary companions.

For the time being, most of these data-driven studies of disk evolution are somewhat piecemeal in terms of both diagnostics and target samples, due to practical observational limitations. While that should soon change dramatically with the completion of the Atacama Large Millimeter Array (ALMA) facility, it is important to recognize that some individual targets will always serve as particularly illuminating case studies for different aspects of disk evolution. Here, we focus on the disk around V4046 Sgr, a remarkable system with observable characteristics that are likely simultaneously shaped by *all* of the fundamental processes involved in disk evolution.

V4046 Sgr is a double-lined spectroscopic binary with a 2.4-day orbital period (Byrne 1986; de la Reza et al. 1986; Quast et al. 2000; Stempels & Gahm 2004). Radial velocity monitoring indicates a nearly equal-mass pair of K-type stars on a close ( $a \approx 0.045 \,\mathrm{AU}$ ), circular ( $e \leq 0.001$ ) orbit (Stempels 2013). Kastner et al. (2011) suggested that GSC 07396-00759 could be an additional distant ( $\sim 2.8$ ) companion, which itself might be an unresolved close binary (see also Nataf et al. 2010). Two independent, dynamical methods to estimate the V4046 Sgr stellar masses are in agreement, with  $M_{*,1} = 0.90 \pm 0.05$  and  $M_{*,2} = 0.85 \pm 0.04$  M<sub> $\odot$ </sub> for the primary and secondary, respectively (Rosenfeld et al. 2012; Stempels 2013). Coupling these dynamical mass measurements to the inferred temperatures and luminosities, pre-main sequence evolution models suggest that V4046 Sgr has an age of  $\sim 10\text{-}20 \,\mathrm{Myr}$  (Rodriguez et al. 2010; Donati et al. 2011; Rosenfeld et al. 2012). Those ages are consistent with the conjecture of Torres et al. (2006, 2008) that V4046 Sgr is a member of the  $\beta$  Pic moving group, with a kinematic parallax distance of only 73 pc from the Sun. Evidence for a disk around the V4046 Sgr binary first came from emission line accretion signatures (H $\alpha$ equivalent widths of ~30-120Å; Merrill & Burwell 1950; Henize 1976; Herbig & Bell 1988) and an infrared continuum excess in the IRAS bands (e.g., Johnson 1986; Weintraub 1990; Weaver & Jones 1992). Strong (sub)millimeter emission was detected by Jensen et al. (1996), suggesting a relatively large disk mass. Jensen & Mathieu (1997) modeled the infrared SED and concluded that it was consistent with an extended circumbinary disk truncated at an inner edge radius of  $\sim 0.2 \,\mathrm{AU}$ , as would be expected from dynamical interactions with the central binary (e.g., Artymowicz & Lubow 1994). Later, Kastner et al. (2008) discovered a substantial reservoir of molecular gas in the disk orbiting V4046 Sgr, which was subsequently imaged and found to span  $\sim 800 \,\mathrm{AU}$  in diameter (roughly 10" on the sky; Rodriguez et al. 2010; Oberg et al. 2011; Rosenfeld et al. 2012). Fitting an elliptical Gaussian to their 230 GHz continuum visibilities, Rodriguez et al. (2010) suggested that the mm-wave dust emission is concentrated inside a  $\sim$ 40 AU radius.

Taken together, these properties make the V4046 Sgr system a significant benchmark for studies of protoplanetary disk evolution for three key reasons. First, the advanced age of the disk suggests that evolutionary effects have had more time to progress, and therefore should exhibit more obvious observational signatures than for a typical ~1 Myr-old disk. Evolutionary mechanisms like particle growth and migration (e.g., Birnstiel et al. 2012a), giant planet formation (e.g., Pollack et al. 1996; Hubickyj et al. 2005), and gas dissipation via photoevaporative winds (e.g., Clarke et al. 2001; Alexander & Armitage 2009) should all be relevant in shaping disk properties at the V4046 Sgr age. For reference, such disks are rare: V4046 Sgr harbors the only gas-rich disk in the  $\beta$  Pic moving group, and is one of a handful of gas-rich disks known to be associated with T Tauri stars in local young stellar groups (the others orbit TW Hya, MP Mus, and T Cha; Kastner et al. 1997, 2010; Sacco et al. 2013). Second, the proximity of V4046 Sgr is a substantial practical advantage in measuring key evolutionary diagnostics: the same observations would be  $4\times$  more sensitive and probe 2× smaller spatial scales for V4046 Sgr compared to disks around younger T Tauri stars that are associated with the nearest star-forming clouds (at distances  $\sim 140\,\mathrm{pc}$ ). And third, from the perspective of a stellar host, V4046 Sgr introduces some interesting environmental issues that could influence the evolution of its disk. Aside from dynamical clearing due to its stellar multiplicity, the binary at the center of the V4046 Sgr disk makes for an unusual dichotomy. The combined mass of the two central stars means that dynamical timescales in the disk are relatively short. However, the irradiation environment is not much different than for a single star, so timescales tied to thermal, energetic, or chemical processes are comparatively unaffected. In essence, the evolutionary behavior of the V4046 Sgr disk can be described as a hybrid of a typical Herbig Ae disk and T Tauri disk, depending on the relevant timescale that dominates a given evolution mechanism.

In this article, we present new, sensitive, high angular resolution observations of the 1.3 mm continuum and  $^{12}\text{CO}/^{13}\text{CO}/\text{C}^{18}\text{O}$  J=2-1 line emission from the V4046 Sgr circumbinary disk. Using these data and a suite of radiative transfer tools, we aim to construct a preliminary, representative model of the disk structure in an effort to help characterize the observational signatures of different disk evolution mechanisms. In the following sections, we describe our observations with the Submillimeter Array (SMA) and the relevant data calibration procedures (§2), present some basic observational results (§3), develop models for the disk structure (§4), and comment on their implications for our understanding of disk evolution (§5). A summary is provided in §6.

### 2. Observations and Data Reduction

We observed V4046 Sgr with the Submillimeter Array (SMA; Ho et al. 2004) on Mauna Kea, Hawaii on four occasions in 2009 and 2011. These observations and their calibration were already described by Rodriguez et al. (2010) and Rosenfeld et al. (2012), but a brief summary of the key points is provided here for completeness. In these observations, the individual 6-m array elements were arranged in each of the four available SMA configurations, spanning baseline lengths from 8

to 509 m. The dual-sideband receiver backends and SMA correlator were configured with a local oscillator (LO) frequency of 225.360 GHz (1.33 mm) and a  $\sim$ 2 GHz-wide intermediate frequency (IF) band  $\pm$ 4-6 GHz from the LO: in 2011, a second IF band was included  $\pm$ 6-8 GHz from the LO. Each sideband/IF band combination was composed of 24 spectral chunks of 104 MHz width (although typically only the central 82 MHz are used). In the first IF band, three chunks (in each sideband) were split into 512 spectral channels, to sample the CO isotopologue emission at 200 kHz ( $\sim$ 0.25 km s<sup>-1</sup>) resolution. All other chunks were coarsely split into 32 channels (3.25 MHz each) to observe the continuum. Observations of V4046 Sgr were interleaved with visits to J1924-292 ( $\sim$ 15° away) on a 5-15 minute cycle, as well as J1733-130 (22° away) on a  $\sim$ 45 minute cycle. Additional observations of 3C 454.3 and available planets/satellites (Neptune, Ceres, Callisto) were conducted for calibration purposes. A summary of relevant observational parameters is provided in Table 1.

The visibility data in each IF band and from each SMA observation were calibrated independently using the MIR package, as described by Rosenfeld et al. (2012). After confirming their consistency over all IF/sideband combinations and on overlapping baseline lengths, the continuum data were spectrally averaged. Spectral visibilities that cover each CO isotopologue transition were continuum-subtracted and combined. The overall data quality is exceptional for the SMA and the low declination of V4046 Sgr, due primarily to the excellent observing conditions (precipitable water vapor levels were only ~1 mm throughout all of the observations). Synthesis images were made using the CLEAN deconvolution algorithm in the MIRIAD software package for each emission tracer. For the 1.3 mm continuum, we emphasized the emission on smaller spatial scales with a Briggs robust (-1) weighting scheme, resulting in a map with a  $0''.74 \times 0''.38$  synthesized beam (at P.A. = 14°) and an RMS noise level of 1.0 mJy beam<sup>-1</sup>. Channel maps of the <sup>12</sup>CO line emission were generated with natural weighting to produce a  $1.1 \times 0.9$  beam with an RMS noise level of 40 mJy beam<sup>-1</sup> in 25 binned 0.4 km s<sup>-1</sup> velocity channels, centered on the systemic LSR velocity, +2.87 km s<sup>-1</sup> (Rodriguez et al. 2010). Analogous channel maps of the CO isotopologue lines were made by employing a 0".5 Gaussian taper, producing a slightly larger synthesized beam  $(1".5 \times 1".2)$ and a similar RMS noise level ( $\sim 35 \,\mathrm{mJy\ beam^{-1}}$ ).

## 3. Results

A summarized representation of the SMA observations of V4046 Sgr is provided in Figure 1. The synthesized map of 1.3 mm dust continuum emission is shown in Figure 1(a), with contours starting at 5 mJy beam<sup>-1</sup> (5  $\sigma$ ) and increasing at 10 mJy beam<sup>-1</sup> (10  $\sigma$ ) intervals. The integrated flux density recovered in this map is 283±28 mJy (dominated by a 10% systematic calibration uncertainty), consistent with a reasonable extrapolation from single-dish submillimeter photometry measurements (Jensen et al. 1996). We find the mm-wave emission is concentrated in a bright, narrow ring centered at the mean stellar position ( $\alpha = 18^{\rm h}16^{\rm m}10^{\rm s}49$ ,  $-32^{\circ}47'34''.50$ , J2000; Zacharias et al. 2010), with a double-peaked morphology due to limb brightening at the projected ring ansae (see Andrews et al. 2011a). The apparent rotation between the semi-major axis of the disk and the line

joining the two ansae is mostly an artifact of the uv sampling and is reproduced in our models (see §4.2.3). These emission peaks are separated by 0".75 (~55 AU) and have peak intensities of  $50 \pm 5 \,\mathrm{mJy}$  beam<sup>-1</sup> (dominated by a 10% calibration uncertainty; S/N  $\approx 50$ ). The western peak appears slightly brighter (~5 mJy beam<sup>-1</sup>) than its eastern counterpart, but a proper evaluation of the significance of this discrepancy requires a more detailed analysis (see §5). The emission ring itself is at best only marginally resolved, implying a width smaller than the 0".4 (~30 AU) minor axis of the synthesized beam. Figure 1(b) shows the azimuthally-averaged profile of the real and imaginary continuum visibilities as a function of deprojected baseline length, constructed assuming the disk viewing geometry derived by Rosenfeld et al. (2012) ( $i = 33^{\circ}.5$ , PA= 76°). The visibility amplitudes exhibit the distinctive oscillation pattern that is characteristic of an emission ring, with nulls at ~150 and 350 k $\lambda$ . The zero-spacing amplitude is estimated to be ~315 mJy, suggesting that roughly 10% of the total flux density from the disk was filtered out of the synthesized map in Figure 1(a): presumably that emission is distributed on larger scales with low surface brightness.

These SMA continuum measurements demonstrate that the V4046 Sgr binary joins the growing ranks of stars that host massive protoplanetary "transition" disks (e.g., Andrews et al. 2011a), with a central cavity of radius  $\sim 29 \,\mathrm{AU}$  (see §4.2.3) that is substantially depleted of mm-sized dust particles. This classification is commensurate with the SED for V4046 Sgr, shown in Figure 1(c) and constructed from photometry in the literature (Hutchinson et al. 1990; Weaver & Jones 1992; Jensen et al. 1996; Jensen & Mathieu 1997; Rodriguez et al. 2010; Öberg et al. 2011), the 2MASS (Skrutskie et al. 2006) and IRAS (Beichman et al. 1988) point source catalogs, and an archival Spitzer IRS spectrum. The SED features the standard signature of a transition disk, with a distinctive "dip" in the continuum near  $10 \,\mu \mathrm{m}$  suggesting that small, warm dust is preferentially depleted (although not absent; see §4.2.1) near the central binary. An accurate determination of the size of this putative cavity from the SED alone is not trivial (e.g., Calvet et al. 2002), although the very weak excess in the near-infrared makes it clear that the dust optical depths must be significantly diminished within at least a few AU of the central stars. Note that the observed dip in the continuum covers a much wider wavelength range than was inferred by Jensen & Mathieu (1997). Simulations of interactions between a stellar binary and its circumbinary disk suggest that the disk material should be inwardly truncated at a radius  $\sim 2-5 \times$  the binary separation (e.g., Artymowicz & Lubow 1994): for V4046 Sgr, the disk truncation should occur at ~0.2 AU, much smaller than the continuum data suggest. Therefore, the observed dust cavity is not related to interactions with the central binary.

The gas phase of the V4046 Sgr disk traced by CO isotopologue emission lines is represented in Figures 1(d)-(f). The  $^{12}$ CO and  $^{13}$ CO  $J{=}2{-}1$  emission are displayed as moment maps in Figures 1(d) and (e). The velocity-integrated intensities (0th moment) are shown as contours at  $3\,\sigma$  intervals, starting at  $2\,\sigma$  (RMS noise levels are 0.08 Jy beam $^{-1}$  km s $^{-1}$  for  $^{12}$ CO, 0.05 Jy beam $^{-1}$  km s $^{-1}$  for  $^{13}$ CO), overlaid on the intensity-weighted velocities (1st moment), with colors marking the velocity shift relative to line center. These maps exhibit the standard pattern of rotation, more clearly manifested in the individual channel maps shown together in Figure 2. Line emission is

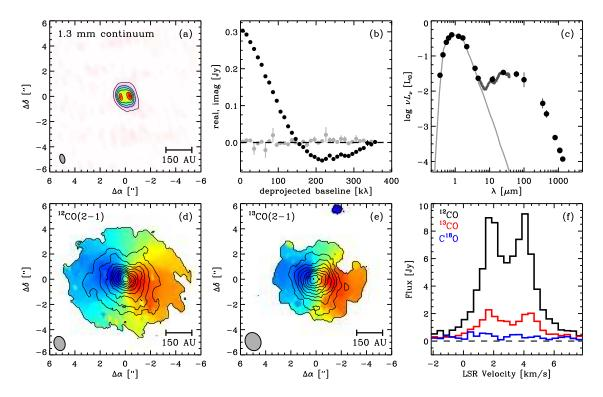


Fig. 1.— An observational summary of the V4046 Sgr disk. (a) An image of the 1.3 mm dust continuum emission, with contours drawn at  $10\,\mathrm{mJy}$  beam<sup>-1</sup> ( $10\,\sigma$ ) intervals, starting at  $5\,\mathrm{mJy}$  beam<sup>-1</sup>. The synthesized beam is shown in the lower left corner. (b) The azimuthally averaged real (black) and imaginary (gray) components of the 1.3 mm continuum visibilities as a function of deprojected baseline length. (c) The broadband SED, with a composite photosphere model for the two stars marked as a thin gray curve (see Rosenfeld et al. 2012). The thick gray curve shows the Spitzer IRS spectrum. (d) The velocity-integrated intensities (0<sup>th</sup> moment; contours) overlaid on the intensity-weighted velocities (1<sup>st</sup> moment; colors) for the <sup>12</sup>CO J=2-1 line emission. Intensity contours start at 0.16 Jy beam<sup>-1</sup> km s<sup>-1</sup> and increase in 0.24 Jy beam<sup>-1</sup> km s<sup>-1</sup> steps, and the color scale spans an LSR velocity width of  $\pm 3\,\mathrm{km}\,\mathrm{s}^{-1}$  from the systemic value. (e) The same as (d), but for the <sup>13</sup>CO J=2-1 line emission. Intensity contours are drawn at 0.15 Jy beam<sup>-1</sup> km s<sup>-1</sup> intervals, starting at 0.10 Jy beam<sup>-1</sup> km s<sup>-1</sup>. (f) The integrated line profiles of the <sup>12</sup>CO (black), <sup>13</sup>CO (red), and C<sup>18</sup>O J = 2 - 1 (blue; not detected) emission inside square regions 12" on a side.

firmly detected (>3 $\sigma$ , or 0.12 Jy beam<sup>-1</sup> in each 0.4 km s<sup>-1</sup> channel) out to  $\pm 4.4$  or  $\pm 4.0$  km s<sup>-1</sup> from the line center for <sup>12</sup>CO and <sup>13</sup>CO, respectively. Given the V4046 Sgr stellar mass and disk inclination angle ( $i=33^{\circ}.5$ , PA= 76° with an ambiguity in the absolute orientation; Rosenfeld et al. 2012), those maximal projected velocities correspond to disk radii of ~25-30 AU, which is similar to the size of the dust cavity. Therefore, these data do not have sufficient sensitivity in the line wings to rule whether or not there is CO inside the dust cavity. The integrated line intensities derived from the 0<sup>th</sup> moment maps are 34.5  $\pm 3.5$  Jy km s<sup>-1</sup> for <sup>12</sup>CO and 9.4  $\pm$  0.9 Jy km s<sup>-1</sup> for <sup>13</sup>CO.

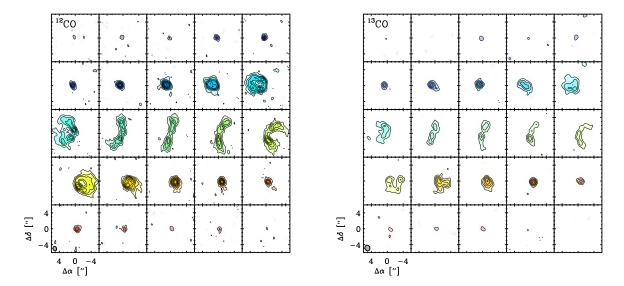


Fig. 2.— Naturally weighted channel maps of the  $^{12}$ CO J=2-1 (*left*) and  $^{13}$ CO J=2-1 (*right*) emission towards the V4046 Sgr disk. Channels are  $0.4 \,\mathrm{km\ s^{-1}}$  wide with the synthesized beam marked in the bottom left corner. Contour levels are drawn at intervals of  $0.12 \,\mathrm{Jy\,beam^{-1}}$  ( $3\,\sigma$ ).

The peak intensities in the channel maps are  $0.95 \pm 0.10 \,\mathrm{Jy~beam^{-1}}$  ( $22 \pm 2 \,\mathrm{K}$ ; peak S/N  $\sim 20$ ) and  $0.47 \pm 0.08 \,\mathrm{Jy~beam^{-1}}$  ( $6.5 \pm 0.8 \,\mathrm{K}$ ; peak S/N  $\sim 11$ ), respectively. The C<sup>18</sup>O emission is faint, and at best only marginally detected. We estimate an integrated intensity of  $\sim 0.6 \,\mathrm{Jy~km~s^{-1}}$  from a 0<sup>th</sup> moment map, but suggest that this number be treated with caution: there is no firm detection in individual channel maps. For reference, spatially integrated spectra for the CO isotopologue lines are shown together in Figure 1(f).

One of the notable features of Figure 1 is the disparity in the apparent spatial extents of the CO line and dust continuum emission. The optically thick  $^{12}$ CO line emission spans a diameter of 10" on the sky, corresponding to a projected disk radius of  $\sim 365$  AU. Comparing Figures 1(a) and (d), we find the dust ring extent is roughly  $5\times$  smaller. The fainter, optically thinner  $^{13}$ CO emission still subtends  $\sim 8$ " on the sky,  $\sim 4\times$  larger than the 1.3 mm continuum.

#### 4. Modeling Analysis

Having highlighted the basic observational characteristics of the gas and dust tracers in the V4046 Sgr circumbinary disk, we now move to a more quantitative effort to explore what the data can tell us about the disk structure. We concentrate our analysis on extracting a model for the radial distributions of gas and dust based on the observational results described in §3. To do that, we first describe a flexible modeling framework for constructing disk structures given an arbitrary surface density profile and dust-to-gas ratio (§4.1), generalized from a similar analysis of the TW Hya disk (Andrews et al. 2012). Using this formalism, we then consider in turn the SED

and the resolved 1.3 mm continuum observations and present model disk structures that optimally account for these data (§4.2.1 and 4.2.2) under the assumption of a constant dust-to-gas ratio. After weighing the successes and failures of these two models, we relax the latter assumption and construct a model (§4.2.3) that is more consistent with all of the data: the broadband SED, the resolved dust continuum emission, and the resolved line emission from two CO isotopologues. The ultimate success of this latter model provides some insights on the shortcomings of our typical assumptions when analyzing disk structures, which are discussed further in §5.

#### 4.1. Physical and Practical Overview

Here we describe a generic prescription for constructing a parametric model of the twodimensional density and temperature structure of both dust and gas in a protoplanetary disk, which builds on the previous work by Andrews et al. (2009, 2010, 2011a, 2012). We assume an axisymmetric, two-dimensional model in a cylindrical reference frame with coordinates (r, z).

Since dust grains dominate the opacity in a disk, we construct a model starting with the distribution of its constituent solids. In a general case with different dust populations, the density distribution is simply defined as the discrete sum  $\rho_{\text{dust}}(r,z) = \sum_{j} \rho_{j}(r,z)$ , where

$$\rho_j(r,z) = \frac{\Sigma_j(r)}{\sqrt{2\pi}H_j(r)} \exp\left[-\frac{1}{2}\left(\frac{z}{H_j(r)}\right)^2\right]. \tag{1}$$

In Eq. (1),  $\Sigma_j(r)$  is the surface density profile and  $H_j(r)$  is the scale height profile for each dust population (labeled by index j). To keep the problem tractable, we consider only two dust populations in this study: a "midplane" population that dominates the disk mass and is composed of larger grains that are vertically settled, and a less-abundant "atmosphere" population of smaller grains that is distributed to larger heights from the midplane. We define parametric scale height profiles

$$H_{\rm atm}(r) = H_0 (r/r_0)^{\psi} \tag{2}$$

$$H_{\text{mid}}(r) = \chi H_{\text{atm}}(r),$$
 (3)

where  $H_0$  is the scale height at  $r=r_0$ ,  $\psi$  is the flaring index, and  $\chi$  is a scaling factor (in the range 0 to 1) that mimics dust settling: we assign a fixed  $\chi=1/2$  for simplicity. The absorption and scattering opacities for each dust population were computed with a Mie code, assuming segregated spherical particles with the Pollack et al. (1994) mineralogical composition and optical constants and a size distribution  $n(a) \propto a^{-3.5}$  between 5 nm and a maximum size (here a is the grain radius). In this specific case, we fix  $a_{\text{max}}(\text{atm}) = 10 \,\mu\text{m}$  and  $a_{\text{max}}(\text{mid}) = 1 \,\text{cm}$ , which reproduces the shape of the (sub)mm-wavelength SED well (see models described in §4.2.1, 4.2.2, and 4.2.3).

For any functional form for the surface densities,  $\Sigma_j(r)$ , the two-dimensional distribution of dust densities (and optical depths, accounting for the grain properties) can be specified with

the above prescription. Given  $\rho_{\rm dust}(r,z)$ , we calculate the corresponding temperature structure,  $T_{\rm dust}(r,z)$ , using the Monte Carlo radiative transfer code RADMC-3D<sup>1</sup>, assuming an incident radiation field from the central binary. For the latter, we use a composite spectrum of two Lejeune et al. (1997) model photospheres with  $\{T_{\rm eff,1}=4350\,{\rm K},\,L_{*,1}=0.35\,{\rm L}_{\odot},\,M_{*,1}=0.90\,{\rm M}_{\odot}\}$  and  $\{T_{\rm eff,2}=4060\,{\rm K},\,L_{*,2}=0.25\,{\rm L}_{\odot},\,M_{*,2}=0.85\,{\rm M}_{\odot}\}$  (for details, see Rosenfeld et al. 2012).

To construct a corresponding gas disk structure, we define a vertically integrated dust-togas mass ratio  $\zeta$  that may vary spatially, such that  $\Sigma_{\rm gas}(r) = \Sigma_{\rm dust}(r)/\zeta(r)$ , where  $\Sigma_{\rm dust}(r) = \sum_j \Sigma_j(r)$ . The two-dimensional density structure of the gas,  $\rho_{\rm gas}(r,z)$ , is determined by numerically integrating the differential equation that describes vertical hydrostatic equilibrium for a given gas temperature distribution,  $T_{\rm gas}(r,z)$  (see Andrews et al. 2012, their Eq. 5). At the midplane (z=0), the gas and dust are assumed to be thermally coupled:  $T_{\rm gas}(r,z=0) = T_m = T_{\rm dust}(r,z=0)$ . At larger vertical heights, the gas temperatures are permitted to deviate from the dust temperatures. To facilitate those departures, we adopt the parameterization introduced by Dartois et al. (2003),

$$T_{\text{gas}}(r,z) = \begin{cases} T_a + (T_m - T_a) \left[ \cos \frac{\pi z}{2z_q} \right]^{2\delta} & \text{if } z < z_q \\ T_a & \text{if } z \ge z_q \end{cases}, \tag{4}$$

where  $T_a = T_{a,0}(r/r_0)^{-q}$  is a parametric temperature profile for the gas in the disk atmosphere, which is explicitly defined here as heights larger than a fiducial value,  $z_q$ . We fix  $z_q = 2H_{\rm gas} = 2c_s/\Omega$ , where  $H_{\rm gas}$  is the hydrostatic gas scale height evaluated at the midplane temperature  $(T_m)$ , defined as the ratio of the sound speed  $(c_s)$  to the Keplerian angular velocity  $(\Omega)$ . The index parameter  $\delta$  determines the shape of the vertical temperature gradient of the gas, and is fixed here to  $\delta = 2$ , following Dartois et al. (2003). Finally, to insure a physically realistic model, we impose the additional criterion that the gas cannot be colder than the dust: if  $T_{\rm gas}(r,z)$  calculated using Eq. (4) is less than  $T_{\rm dust}(r,z)$  computed from the radiative transfer simulation, we set  $T_{\rm gas} = T_{\rm dust}$ . In practice, this formulation provides a straightforward means of permitting extra gas heating relatively near the star, while (if desired) maintaining thermal coupling between the gas and dust at all heights at large disk radii ( $r \gtrsim 100 \, {\rm AU}$ ; see §4.2). For the kinematic structure of the disk, we assume the gas is in Keplerian rotation around the central stars,  $v_{\theta}^2 = GM_*/r$ , and that the emission line profile widths are determined from the quadrature sum of a thermal and turbulent broadening term, with a fixed and constant value for the latter of  $\xi = 0.1 \, {\rm km \ s^{-1}}$ .

Having defined the gas disk structure, we need to assign an abundance distribution for the tracer molecule, CO. Following Aikawa & Herbst (1999), we assume that 80% of the gas is composed of  $H_2$  and then assume a *constant* fractional abundance  $f_{co} = n(^{12}CO)/n(H_2)$  such that

$$n(^{12}CO) = 0.8 f_{co} \frac{\rho_{gas}(r,z)}{\mu m_{H}}$$
 (5)

in the region of the disk we term the "abundant layer". In Eq. (5),  $\mu$  is the mean molecular weight of the gas ( $\mu = 2.37$ ) and  $m_{\rm H}$  is the mass of a hydrogen atom. The abundant layer is defined based

<sup>1</sup>http://www.ita.uni-heidelberg.de/\$\sim\$dullemond/software/radmc-3d/

on the treatment of Qi et al. (2008, 2011), which assumes CO is present in the gas phase if: (1) the local gas temperatures are high enough that the CO is not frozen onto the dust grains, and (2) the vertically-integrated column density is higher than the penetration depth of photodissociating radiation. At each radius, Eq. (5) is used to compute the CO densities if

$$T_{\text{frz}} \leq T_{\text{gas}}(r, z)$$
 (6)

$$\sigma_s \leq f_{\rm H} \int_z^\infty n_{\rm gas}(r, z') dz'$$
 (7)

are valid: here,  $T_{\rm frz}$  is the CO freezeout temperature,  $\sigma_s$  is the photodissociation column, and  $f_{\rm H}$  is the fraction of H nuclei in the gas. Guided by Aikawa & Herbst (1999) and Qi et al. (2011), we assume  $f_{\rm H}=0.706$  and fix  $T_{\rm frz}=19\,\rm K$  and  $\sigma_s=5\times10^{20}\,\rm cm^{-2}$ . At locations where Eqs. (6) and (7) are not met, we sharply (and arbitrarily) reduce the <sup>12</sup>CO abundance by scaling  $f_{\rm co}$  down by a factor of  $10^8$ . The CO isotopologue abundances are assumed to follow <sup>12</sup>CO with the interstellar medium ratios inferred by Wilson (1999):  $n(^{12}{\rm CO})/n(^{13}{\rm CO})=69$  and  $n(^{12}{\rm CO})/n(^{18}{\rm CO})=557$ .

The formalism described above and encapsulated in Eqs. (1)-(7) fully defines the dust and gas structure of a model disk. In practice, the dust structure depends on some description of the surface density profiles for each dust species,  $\Sigma_i(r)$ , and their corresponding vertical height profiles,  $H_i(r)$ : here, the latter is fully specified with two parameters,  $\{H_0, \psi\}$ . Likewise, the gas structure is determined by a dust-to-gas mass ratio profile  $\zeta(r)$ , and three additional free parameters:  $\{T_{a,0},$ q} to define the atmosphere temperature profile and  $\{f_{co}\}$  to assign the CO molecular abundance. For a given model, we generate synthetic data products to compare with the observations and evaluate our parameter choices and the underlying model characterization. For the dust, we use the ray-tracing capability of RADMC-3D to produce a synthetic SED and set of 1.3 mm continuum visibilities sampled at the same spatial frequencies as observed by the SMA. For the gas, we use the molecular excitation and line radiation transfer code LIME (Brinch & Hogerheijde 2010) to calculate the non-local thermodynamic equilibrium level populations based on information from the LAMDA database (Schöier et al. 2005) and then calculate synthetic spectral visibilities for each of the CO isotopologues in the velocity channels and spatial frequencies sampled by the SMA. In all models, we assume the disk inclination  $(i = 33^{\circ}.5)$ , major axis position angle (PA =  $76^{\circ}$ ), total stellar mass  $(M_* = 1.75 \,\mathrm{M}_{\odot})$ , and disk center position derived by Rosenfeld et al. (2012), as well as the distance  $(d = 73 \,\mathrm{pc})$  inferred by Torres et al. (2006, 2008).

#### 4.2. Model Results

The modeling framework we have constructed is relatively complex, with some fairly severe parameter degeneracies (for a more detailed discussion, see Andrews et al. 2009, 2011a, 2012; Qi et al. 2011). Moreover, the computational effort required for the radiative transfer and non-LTE excitation calculations remains costly, severely limiting our capability to use either stochastic or deterministic optimization algorithms to robustly probe the parameter-space. In practice, we build

structure models manually, using small explorations of each parameter to reproduce the key observational features of interest. This means that the models presented below are not quantitatively optimized, nor unique. However, they are still of great interest since they serve as qualitative illustrations of key features in the V4046 Sgr disk structure that are not otherwise easily accessible. In the following sections (§4.2.1 and 4.2.2), we aim to provide a pedagogical guide to the logic behind the more complex disk structure we ultimately will advocate for the V4046 Sgr disk (§4.2.3).

#### 4.2.1. Model to Reproduce the SED

As a starting point, we focus on building a structure model that is designed to reproduce the broadband SED of V4046 Sgr, with some input from the CO observations to guide our description of the gas disk structure. Following the modeling prescription for transition disks described by Andrews et al. (2011a), we adopt a truncated version of the Lynden-Bell & Pringle (1974) similarity solution for a thin, Keplerian accretion disk with a time-independent, power-law viscosity profile to describe the surface densities of the dust (see also Hartmann et al. 1998),

$$\Sigma_{\text{dust}}(r) = \begin{cases} \Sigma_{ss}(r) = \Sigma_c \left(\frac{r}{r_c}\right)^{-\gamma} \exp\left[-\left(\frac{r}{r_c}\right)^{2-\gamma}\right] & \text{if } r \ge r_{\text{cav}} \\ \Sigma_{\text{cav}} & \text{if } r_{\text{in}} \le r < r_{\text{cav}} \end{cases}, \tag{8}$$

where  $r_c$  is a characteristic radius,  $\gamma$  is an index parameter,  $\Sigma_c = e \cdot \Sigma_{\rm dust}(r_c)$ ,  $r_{\rm cav}$  is a "cavity" radius,  $\Sigma_{\rm cav}$  is a constant, and  $r_{\rm in}$  is the inner edge of the model. Both grain populations were forced to follow the behavior in Eq. (8): outside the disk cavity, 90% of the mass was apportioned to the midplane grains ( $\Sigma_{\rm mid} = 0.9 \, \Sigma_{\rm dust}$ ,  $\Sigma_{\rm atm} = 0.1 \, \Sigma_{\rm dust}$ , for  $r \geq r_{\rm cav}$ ), but the tenuous material inside the cavity was assumed to be all atmosphere grains ( $\Sigma_{\rm mid} = 0$ ,  $\Sigma_{\rm atm} = \Sigma_{\rm cav}$ , for  $r < r_{\rm cav}$ ). Since the SED is composed of unresolved photometric measurements, it has no ability to constrain the gradient  $\gamma$ . Therefore, we fixed  $\gamma = 1$ , a typical value for disks (Andrews et al. 2009, 2010). The inner radius of the model was set to  $r_{\rm in} = 0.2 \, {\rm AU}$ , the outer edge of the zone expected to be cleared by dynamical interactions with the central binary (Artymowicz & Lubow 1994). For the gas phase, we assumed a standard, spatially uniform dust-to-gas ratio,  $\zeta(r) = \zeta = 0.01$  (Pollack et al. 1994; D'Alessio et al. 2001).

After some iteration between dust and gas structures, we identified a model that can reproduce well both the broadband SED and SMA observations of CO line emission: the results are highlighted in Figure 3. Using the morphology of the continuum "dip" in the infrared SED, we inferred a cavity radius  $r_{\rm cav} = 3\,\mathrm{AU}$ , roughly  $15\times$  larger than could be explained by tidal stripping from the V4046 Sgr binary. As with most other transition disks, this cavity is not empty: the weak infrared excess (and weak silicate emission feature) noted in Fig. 3b is accommodated with  $\Sigma_{\rm cav} \approx 10^{-4}\,\mathrm{g}~\mathrm{cm}^{-2}$ . In the mid-infrared, the excess spectrum was fit with a scale height of  $H_0 = 0.4\,\mathrm{AU}$  at  $r_0 = 10\,\mathrm{AU}$  and a flaring index  $\psi = 1.25$  (although the latter is not well-determined in transition disks; see Andrews et al. 2011a). The total mass of the dust structure (the integral of Eq. 8 over the disk area) was  $M_{\rm dust} \approx 9 \times 10^{-4}\,\mathrm{M}_{\odot}$ , determined from the luminosity of the millimeter-wave SED.

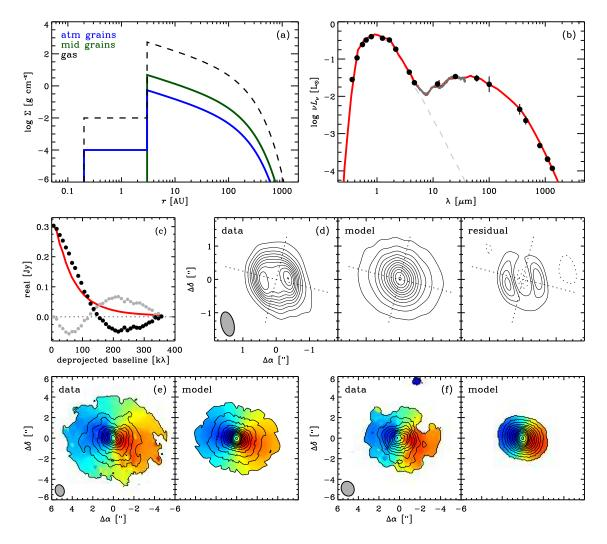


Fig. 3.— Results for the modeling effort focused on the SED (§4.2.1). (a) Surface density profiles for the gas (dashed), the large "midplane" (green) and small "atmosphere" (blue) grain populations. (b) The SED (black points and solid gray curve) compared with the model (red). The stellar photosphere model is shown as a dashed gray curve. (c) The deprojected, azimuthally-averaged (real) 1.3 mm continuum visibility profile, with model overlaid (in red); gray points mark the residuals. (d) The observed, simulated, and residual 1.3 mm emission synthesized maps. Contours are drawn at 5 mJy beam<sup>-1</sup> (5  $\sigma$ ) intervals. Note the smaller map size compared to Figure 1. (e) A comparison of the observed and simulated <sup>12</sup>CO moment maps. (f) The same as panel (e), but for the <sup>13</sup>CO line. Contour levels and map sizes for panels (e) and (f) are the same as in Figure 1.

The characteristic size of the disk was estimated to be  $r_c = 75\,\mathrm{AU}$ , based on the extent of the  $^{12}\mathrm{CO}$  emission. Those data were described well with a CO abundance  $f_{\mathrm{co}} = 3 \times 10^{-6}$  and a steep atmospheric temperature profile with  $T_0 = 200\,\mathrm{K}$  (at  $r_0 = 10\,\mathrm{AU}$ ) and q = 0.8. In practice, this  $T_a(r)$  profile means the gas and dust are thermally coupled for  $r \gtrsim 150\,\mathrm{AU}$ , but there is some

source of additional gas heating in the disk atmosphere at smaller radii. One possible source for that heating is the strong X-ray emission from the central binary (see §5).

Although by design this model provides a good match to the SED and CO emission, it should be obvious from Figure 3 that it is irreconcilable with the resolved 1.3 mm continuum data. However, these failures are instructive in refining the model. The residuals in Figures 3(c)-(d) point out two key issues. First, the cavity size derived from the SED alone substantially under-estimates the size that can be directly measured from the resolved 1.3 mm data. In §3, we estimated a cavity radius of  $\sim$ 29 AU (and will quantify that further below),  $\sim$ 10× larger than derived here. This kind of discrepancy is not uncommon for transition disks (e.g., DM Tau; Andrews et al. 2011a): any inference of a size scale from unresolved observations is inherently uncertain and may be a signature of how the dynamics of grains depends upon their size (see §5). Second, the spatial extent of this model is much larger than the 1.3 mm continuum distribution. This latter point is manifested in the poor match to the visibility profile in Figure 3(c) on large spatial scales (short baselines), where the model is clearly more resolved than the data permit (the negative residuals outside the emission ring in Figure 3(d) represent the same aspect of this model failure). Since  $r_c$  was determined from the CO data, this discrepancy is not surprising: we already highlighted in §3 how the CO emission is much more extended than the dust emission (see Fig. 1).

#### 4.2.2. Model to Reproduce the Resolved 1.3 mm Continuum Emission

Informed by the failures of the previous model, we shift the focus here to building a model that is more consistent with the resolved morphology of the 1.3 mm dust emission. Two prescriptions for the surface density profile are presented, both of which can reproduce the size and shape of the mm-wave emission. Considering the visibility profile (Fig. 1a), the former is constrained by the short baselines ( $\mathcal{R} \lesssim 150 \,\mathrm{k}\lambda$ ) and the latter is dictated by the position of the null and deep trough at higher spatial frequencies. The results shown in Figure 4 are for the same relative ratios of midplane and atmosphere grains and model parameterization defined in §4.2.2, but with the the cavity size,  $r_{\rm cav}$ , enlarged to 21 AU (i.e., adjusted without regard to the infrared SED). In addition, this model has  $\gamma = -1.5$ ,  $r_c = 45 \,\text{AU}$ ,  $\psi = 1.5$ ,  $H_0 = 0.45 \,\text{AU}$  at  $r_0 = 10 \,\text{AU}$ , and  $0.0011 \,M_{\odot}$  of dust. Note that a negative  $\gamma$  implies a density profile that rises with radius out to  $r_c$ , but then is sharply truncated. In essence, it naturally produces a relatively narrow "ring" of material (Isella et al. 2009), making it a practical means of describing the resolved morphologies of transition disks (e.g., Isella et al. 2010, 2012; Andrews et al. 2011b; Brown et al. 2012). We also consider an alternative parameterization of the surface density profile where the viscous disk similarity solution,  $\Sigma_{\rm dust}(r) = \Sigma_{ss}(r)$  (see Eq. 8), is valid for all r. Figure 5 summarizes this second model which features a large, negative  $\gamma = -3.5$  with  $r_c = 48$  AU,  $\psi = 1.5$ ,  $H_0 = 0.4$  AU at  $r_0 = 10$  AU and  $0.0010 \, M_{\odot}$  of dust.

Although both of these models reproduces well the morphology of the 1.3 mm emission ring (Figs. 4,5c,d), they each fail to account for the observations of the V4046 Sgr disk in three similar, illuminating ways. We also experimented with alternative prescriptions for the surface densities

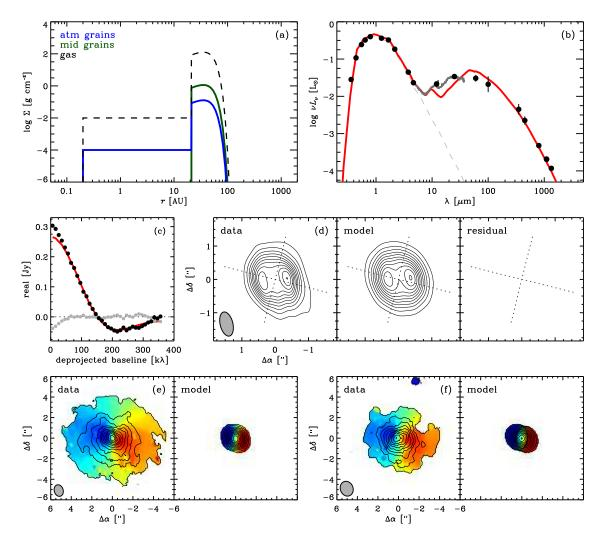


Fig. 4.— Results for the modeling effort focused on the resolved 1.3 mm dust continuum emission (first model described in §4.2.2). See Figure 3 for a description of the contents of individual panels.

(e.g., a power-law with an outer edge cut-off), and found qualitatively similar results. First, they produce too deep and wide of a "dip" in the infrared SED in Figures 4,5(b), because there is not enough dust interior to the density peak. Note that the mid/far-infrared excess of the models is a manifestation of this lack of inner disk material: in the absence of an inner disk, a larger surface area of more distant material in the model ring can be directly illuminated by the central stars, producing a "bump" in the continuum at  $\sim 50 \,\mu\text{m}$ . Second, if we assume a standard, uniform dust-to-gas ratio as before ( $\zeta = 0.01$ ), there is not enough gas outside the density peak in either of these models to account for the observed spatial extent of the CO emission (Figs. 4,5e,f). For a constant  $\zeta$ , this size discrepancy is present regardless of the assumed CO abundance or gas temperature distribution, although the results in Figures 4 and 5 use the same  $f_{\text{co}}$  and  $f_{\text{co}}$  and  $f_{\text{co}}$  that were adopted

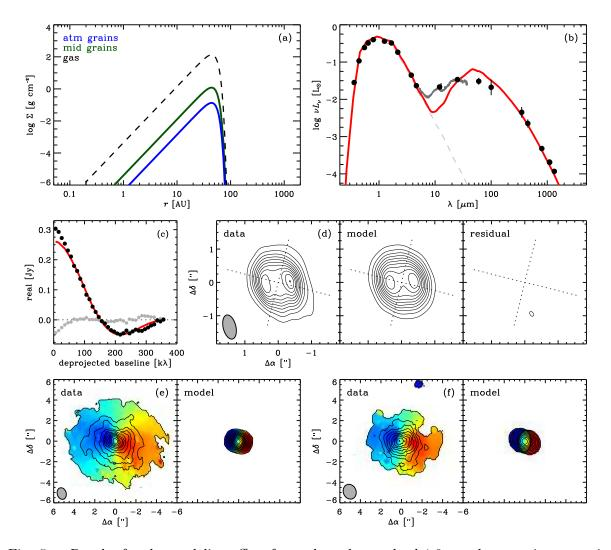


Fig. 5.— Results for the modeling effort focused on the resolved 1.3 mm dust continuum emission (second model described in §4.2.2). See Figure 3 for a description of the contents of individual panels.

in §4.2.1. And third, the models do not quite generate enough 1.3 mm dust emission on large angular scales (deprojected baselines  $\leq 50 \,\mathrm{k}\lambda$ ; see Figs. 4,5c). The origins of this last discrepancy are indeed subtle. We are unable to account for all the emission through a simple scaling of the dust mass because the model ring is already nearly optically thick (this is exacerbated by our assumption of isotropic scattering off large, spherical grains). Increasing the densities further effectively impedes the radiation transfer to the midplane, making the dust cooler and actually decreasing the 1.3 mm luminosity. Instead, we interpret this emission mismatch as an intrinsic model deficiency: the addition of a low-density, spatially-extended dust component could reconcile the model visibilities with the data. Note that this faint ( $\sim 10$ -15% of the total flux) emission "halo" would be strongly spatially filtered in the synthesized images, as was found for the SMA observations in §3.

### 4.2.3. A Hybrid Model to Reproduce All the Data

The three different models constructed above illustrate the key features of the V4046 Sgr disk structure. To review those results, we have identified three basic structural elements that are required in any model prescription that aims to successfully reproduce the observations:

- 1. The vast majority of the large grain population must be strongly concentrated in a *narrow* ring with a large central cavity to explain the 1.3 mm continuum visibilities;
- 2. Inside that cavity, a reservoir of small dust particles (which produce little mm-wave emission) at radii of a few AU are required to account for the morphology of the infrared SED;
- 3. A large-scale, extended halo structure is necessary to explain the CO line emission size and a faint, strongly spatially filtered 1.3 mm continuum component, but there appears to be substantially less mass in the large dust particles relative to the gas outside the concentrated ring component.

Here, our goal is to combine the successful aspects of the models described above into a hybrid structure that incorporates these three elements and is commensurate with all of the observations.

We define a surface density profile for the dust that is composed of three individual components, each corresponding to one of the structural elements enumerated above:

$$\Sigma_{\text{dust}}(r) = \Sigma_{\text{ring}}(r) + \Sigma_{\text{in}}(r) + \Sigma_{\text{halo}}(r). \tag{9}$$

We elect to use simple Gaussian profiles for the distribution of material in the ring and inner disk components,

$$\Sigma(r) = \frac{\Sigma_0}{\sqrt{2\pi}\sigma} \exp\left[-\frac{1}{2} \left(\frac{r-\mu}{\sigma}\right)^2\right],\tag{10}$$

where we define parametric constants that correspond to peak radii  $\{\mu_{\rm ring}, \mu_{\rm in}\}$ , profile widths  $\{\sigma_{\rm ring}, \sigma_{\rm in}\}$ , and normalizations  $\{\Sigma_{0,\rm ring}, \Sigma_{0,\rm in}\}$  for both structure components separately. We assume that the ring component is composed solely of the large "midplane" grains, and that the inner component is made up entirely of the small "atmosphere" grains. For the halo component, we again assume a truncated similarity solution model (as in §4.2.1), but eschew the sharp inner edge for one with a smoother, Gaussian taper:

$$\Sigma_{\text{halo}}(r) = \Sigma_{ss}(r; \{\Sigma_c, r_c, \gamma\}) \exp\left[-\left(\frac{\mu_{\text{ring}}}{r}\right)^2\right]. \tag{11}$$

The functional form of Eq. (11) is arbitrary, and was selected entirely for purposes of convenience in the radiative transfer modeling (tying the exponential turnover scale to the ring component center makes a joint exploration of the model space less cumbersome). We fix  $\gamma = 1$  as before and use a 6:1 mass ratio between the midplane and atmosphere grains. The gas is assumed to follow the

small grains in both the halo and inner disk components separately – i.e. decoupled from the large grain population – each with a ratio  $\zeta$ . We use the halo gas profile as an upper limit on the surface density of midplane grains in the ring. For radii where the ratio between the two would exceed unity (e.g. in the space between the two Gaussian distributions), we reduce  $\Sigma_{\text{ring}}$  to equal the gas surface density from the halo component. Either increasing the gas or reducing the dust density has no significant effect upon our observables since the subtended region is very narrow and the densities are already low.

A model constructed with the recipe outlined above is superior to those presented in §4.2.1 and 4.2.2 in terms of reproducing all the relevant observations of the V4046 Sgr transition disk, as demonstrated in Figure 6. In this case, we assumed that the same dust scale height distributions used in the previous sections were applicable to all of the structure elements. For the ring component, we identify its center at  $\mu_{\rm ring} = 37\,{\rm AU}$  and width  $\sigma_{\rm ring} = 7\,{\rm AU}$  (corresponding to a FWHM of 16 AU, or 0", 2 projected on the sky; notably smaller than the SMA angular resolution), and allocate a large total dust mass of  $0.004\,\mathrm{M}_{\odot}$ . The representative size of the central cavity is estimated to be 29 AU by subtracting one half of the FWHM from the ring radius. In the inner disk, we find  $\mu_{\rm in} = 4\,{\rm AU}$ ,  $\sigma_{\rm in} = 1\,{\rm AU}$ , and a total dust mass of  $2\times10^{-5}\,{\rm M}_{\odot}$ . To account for the faint, extended 1.3 mm emission component and the size of the CO emission, a halo component with a characteristic radius  $r_c = 75\,\mathrm{AU}$  and total dust mass of  $\sim 10^{-4}\,\mathrm{M}_\odot$  is sufficient. To produce sufficient CO line intensities for the same gas temperature and molecular abundance structures highlighted in §4.2.1, we set  $\zeta = 0.0014$  in the outer disk, relative to the halo component only. The weak  $C^{18}O$  emission of this model is consistent with the observations (i.e. a non-detection). In the inner disk, we have kept  $\zeta = 0.01$  fixed as before. The total (gas+dust) mass in this model is  $\sim 0.094 \,\mathrm{M}_{\odot}$  and the disk-integrated dust-to-gas mass ratio is  $\sim 0.047$ .

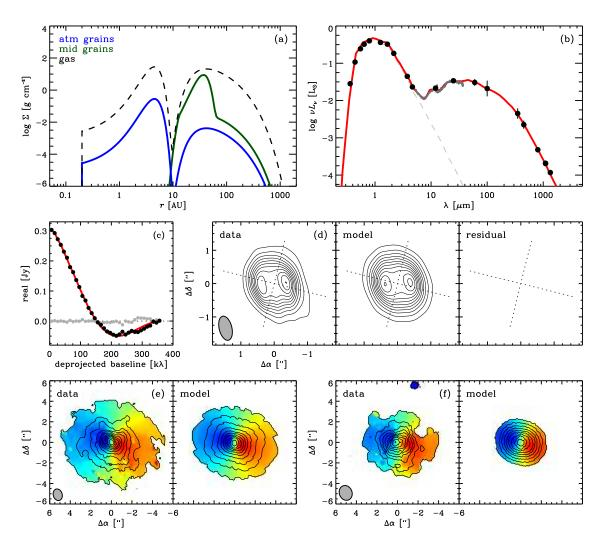


Fig. 6.— Results for the modeling effort that successfully reproduces all of the data (SED, 1.3 mm continuum visibilities, and CO spectral images). See Figure 3 for descriptions of individual panels.

#### 5. Discussion

We have presented sensitive, high angular resolution SMA observations of the 1.3 mm dust continuum and spectral lines of three CO isotopes from the V4046 Sgr circumbinary disk. We have modeled the dust and gas structures and identified three fundamental signatures of profound evolution in this disk. First, the majority of the large grains are distributed in a narrow ring centered creating a large central cavity ( $r \sim 29\,\mathrm{AU}$ ). Second, there exists a significant population of  $\mu$ m-sized grains that have not been cleared from the center of this cavity. Third, the gas disk extends much farther than the compact dust ring, suggesting that this disk has a radial variation in the dust-to-gas mass ratio.

To explain the striking discrepancy between the size of the gas and dust distributions, we invoke a model with a strong radial variation in the relative mass ratio of the large, midplane grains and the gas. The dust-to-gas mass ratio in the model is large at the dust ring ( $\zeta \sim 0.1-1$ ) and small outside of it ( $\zeta \sim 10^{-3}$ ). Similar discrepancies between the gas and dust distributions have been noted for other disks, such as those around IM Lup (Panić et al. 2008), TW Hya (Andrews et al. 2012), and LkCa 15 (Isella et al. 2012). While our preferred model does feature an extended, but tenuous, dusty halo, models where the dust uniformly follows the gas disk either produce too much continuum or too little CO emission at large radii and clearly disagree with the observations (see §4.2.1 and §4.2.2). We caution that the model <sup>12</sup>CO and <sup>13</sup>CO line emission is optically thick and so the derived dust-to-gas mass ratios are upper limits. Additionally, the dust mass in the model is sensitive to the dust opacities and so other values of the dust-to-gas mass ratio and total disk mass are possible. The precise form and normalization of  $\zeta(r)$  are model dependent, but the observations seem to suggest that it is a strongly decreasing function.

While the underlying physical cause of the discrepancy between the size of the gas and dust distributions is not clear, there is a natural explanation in the growth and inward radial drift of dust particles (Weidenschilling 1980; Brauer et al. 2008; Birnstiel et al. 2010). Drift is a fundamental feature in the migration of disk solids, generated because the radial pressure gradient in the disk causes the gas to rotate at slightly sub-Keplerian velocities while the dust particles are on Keplerian orbits. The resulting headwind creates a drag-force on the dust that relates to the size of the particle, preferentially moving the large particles towards the central star (Weidenschilling 1977; Takeuchi & Lin 2002). As these particles drift inwards, their size distribution is continuously evolving as they encounter higher local densities that are conducive to growth (Birnstiel et al. 2010). The collective effect is to shrink the radial extent of the dust mass distribution, as the gas disk continues to viscously spread to larger radii (Birnstiel et al. 2012a). Since these processes operate on dynamical timescales, this phenomenon should be particularly pronounced for the V4046 Sgr disk due to the binarity (increased  $M_*$ ) and advanced age of its stellar hosts. Resolved observations taken across the (sub-)millimeter and radio bands may clarify whether the radial grain size distribution is consistent with this drift and particle growth scenario (Guilloteau et al. 2011; Pérez et al. 2012).

In order to reproduce the observed morphology of the mm continuum emission, we required

a model that has its large dust grain population distributed in a narrow ring. This is suggestive of a physical mechanism acting to both concentrate the particles radially and prevent them from moving further into the inner disk. Particle growth alone is insufficient to produce mm-wave cavities (Birnstiel et al. 2012b), but this kind of ring-like dust concentration is a natural consequence of particle evolution models that also employ feedback from a large-scale maximum in the radial pressure gradient of the gas (Pinilla et al. 2012a). The dynamics of the dust particles are strongly dictated by the surrounding gas and while negative radial pressure gradients induce inward radial drift, a positive pressure gradient may stop the dust as it streams towards the star. This pressure maximum forms a "pocket" that collects dust and, if sufficiently broad and high-amplitude, can significantly alter the observed continuum emission (Pinilla et al. 2012b).

While many physical phenomena may generate these particle traps (e.g. Barge & Sommeria 1995; Klahr & Henning 1997; Alexander & Armitage 2007; Johansen et al. 2009), we focus on an origin in the density maximum at a gap edge produced by dynamical interactions between a low-mass companion embedded in the gas disk (Lin & Papaloizou 1979; Goldreich & Tremaine 1980; Crida et al. 2006). Simulations by Pinilla et al. (2012a) produced a ring of large grains in a broad surface density bump exterior to the radius of such a gap. Furthermore, their models of the mutual evolution of the gas and dust predicted a strong radial variation in the dust-to-gas mass ratio (see their Figure 6) with heavily depleted dust densities in the outer disk ( $\zeta \sim 10^{-3} - 10^{-4}$ ) and a large concentration within the trap ( $\zeta \sim 1$ ). Both the ring-shaped surface density profile and radially decreasing dust-to-gas ratio produced by their calculation were necessary features of the model we derived for the V4046 Sgr disk.

Recent models that account for the expected substructure in these ring-like pressure traps suggest that a modest variation in the gas density (peak-to-valley amplitude ratio of  $\gtrsim 1.5$ ) can produce strong azimuthal asymmetries in the dust distribution (Regály et al. 2012; Birnstiel et al. 2013). This phenomenon may be sufficient to qualitatively explain some observations of the "lopsided" emission from some transition disks (e.g. Brown et al. 2009; Mayama et al. 2012; Casassus et al. 2013; van der Marel et al. 2013). As noted in §3, the western peak of the V4046 Sgr dust ring appears slightly brighter than the eastern peak by  $\sim 5\,\mathrm{mJy\,beam^{-1}}$ . We find that this subtle asymmetry is apparent in the continuum visibilities as well, and therefore is not likely to be an artifact of the imaging/deconvolution process. Figure 7 shows a cut of the imaginary component of the complex visibilities binned along the v-axis in the Fourier plane (corresponding to the E-W direction). For a symmetric morphology, the imaginary visibilities should be zero: however, we find a statistically significant deviation in a sinusoid pattern. The asymmetry can be reproduced reasonably well with a faint point source ( $\sim 8\,\mathrm{mJy}$ ) located  $\sim 0''$ .23 to the west of the disk center. However, verification and characterization of this low-level apparent asymmetry beyond such a simple model will require observations with higher resolution and sensitivity.

The ring-shaped dust disk and tentative asymmetry seem to be well-matched to predictions for a large pressure trap generated by a companion interacting with the gas disk. However, the central spectroscopic binary itself is too compact and circular to have dynamically truncated the disk at

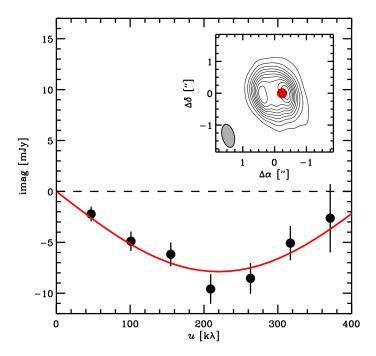


Fig. 7.— The complex visibilities of the 1.3 mm emission binned along the v axis (black points) with a model 8 mJy point source (red) offset by  $\Delta \alpha = -0.23$  from the disk center (red curve). The inset shows the continuum image with 5  $\sigma$  contour levels and the model point source (red dot).

such a large radius: this scenario requires (at least) a third body. One constraint on the properties of a putative companion comes from the dynamical mass estimate by Rosenfeld et al. (2012). Since this method utilizes the Keplerian rotation pattern of the disk, it is sensitive to the cumulative mass at the disk center: the spectroscopic binary plus any other companion(s). If the central binary and disk are co-planar, Rosenfeld et al. (2012) showed that the disk-based dynamical mass estimate was consistent with that inferred from spectroscopic monitoring of the stellar orbits (Stempels 2013). Therefore, any additional companion must have a low mass: the  $3\sigma$  uncertainties on the dynamical mass estimate of Rosenfeld et al. (2012) require that  $M_{\rm comp} \leq 0.3\,{\rm M}_{\odot}$ . A second, complementary constraint can be made from the contribution of any companion to the near-infrared spectrum. The composite stellar photosphere model adopted here accounts for 99, 95, and 85% of the observed emission in the K, L' and M bands, respectively (Jensen & Mathieu 1997; Hutchinson et al. 1990; Skrutskie et al. 2006). If we attribute the remaining emission to a co-eval low-mass companion, rather than the tenuous inner dust ring described in §4, pre-main sequence models (e.g. Baraffe et al. 1998) suggest that the spectrum requires  $M_{\rm comp} \leq 0.2\,{\rm M}_{\odot}$ .

A third constraint on a potential companion was suggested by Donati et al. (2011), based on their claim of a shift in the systemic velocity of the spectroscopic binary. They measured  $V_{\rm sys} = -5.7 \pm 0.2 \, \rm km \, s^{-1}$  (in the heliocentric frame) at a mean epoch of 2009.7, which is significantly different than the previous measurements of the binary ( $-6.94 \pm 0.01 \, \rm km \, s^{-1}$  at epoch 1985.5;

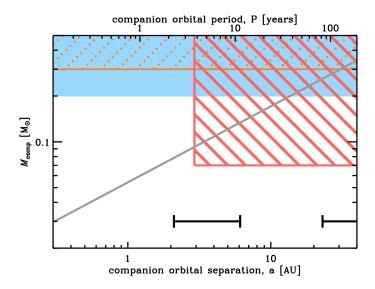


Fig. 8.— Limits on a companion mass with regions ruled out by the dynamical mass estimate (orange dots; Rosenfeld et al. 2012), infrared luminosities (solid blue; Jensen & Mathieu 1997; Hutchinson et al. 1990; Skrutskie et al. 2006), and infrared aperture-masking observations (thick rose lines; A. L. Kraus, private communication). The lower mass limit consistent with the reported velocity shifts is also shown (gray line; Quast et al. 2000; Donati et al. 2011; Rodriguez et al. 2010). The position and  $2\sigma$  widths of the main and inner dust rings are marked by floating error bars.

Quast et al. 2000) and the gas disk  $(-6.26\pm.05\,\mathrm{km\ s^{-1}};\mathrm{Rodriguez}\ \mathrm{et}\ \mathrm{al.}\ 2010)$ . Assuming the total mass determined by Rosenfeld et al. (2012) and co-planar orbits, we can derive a lower limit on the companion mass as a function of semi-major axis (or orbital period) from these apparent velocity shifts:  $M_{\mathrm{comp}} \gtrsim 0.05\,\mathrm{M}_{\odot}(a/1\mathrm{AU})^{1/2}$ , where a is the semi-major axis. It should be noted that these apparent velocity shifts are likely consistent with one another when considering the typical systematic uncertainties in the velocity calibration between different instruments. A final, more direct, constraint on the companion mass can be made from infrared aperture-masking observations (A. L. Kraus; private communication). No companion is detected in those data, with a K-band contrast limit of 6-7 magnitudes outside of 0″.04 from the central binary. Assuming a co-eval companion and the Baraffe et al. (1998) models, these data constrain  $M_{\mathrm{comp}} \leq 0.07\,\mathrm{M}_{\odot}$  for  $a > 2.9\,\mathrm{AU}$ . Figure 8 summarizes these four constraints on  $M_{\mathrm{comp}}$  and a.

Given the results in Figure 8, it is clear that the mass of any companion must be low, making a low-mass brown dwarf or massive giant planet likely candidates. The position of this hypothetical planet from the observed ring is highly uncertain and with no conclusive evidence for reduced densities in the cavity, our CO observations cannot help constrain  $M_{\text{comp}}$  or a. However, sensitive observations with high angular resolution may resolve structure in the inner gas disk (Casassus et al. 2013) or signatures of clearing in the high-velocity wings (Dutrey et al. 2008). An alternative way of locating a companion is by looking at the small grains that filter past it and using this flow of

small grains entrained in the gas to quantify the mass of the companion (Rice et al. 2006; Zhu et al. 2012). While the distribution of  $\mu$ m-sized dust particles in our model are closer to the central binary than the inner working angle of the SEEDS survey (Tamura 2009, 0".1-0".15), the V4046 Sgr disk is a natural candidate to test this scenario with scattered light observations (e.g. Dong et al. 2012).

A compelling potential alternative mechanism for shaping the distinctive structure of the V4046 Sgr disk is photoevaporation (Hollenbach et al. 1994; Clarke et al. 2001; Alexander et al. 2006a,b; Owen et al. 2012) which can also create large pressure traps (Alexander & Armitage 2007). Strong photoionizing radiation from the central stars drive a wind off the disk surface, and consequently can open a gap in the disk on ~AU scales. V4046 Sgr has a large UV excess (de la Reza et al. 1986; Hutchinson et al. 1990; Huenemoerder et al. 2007) and large X-ray luminosity  $(L_X \sim (7-10) \times 10^{29} \,\mathrm{erg \ s^{-1}})$ , based on archival XMM data; see also Günther et al. 2006; Argiroffi et al. 2012). According to recent models (Gorti & Hollenbach 2009; Gorti et al. 2009; Owen et al. 2010, 2011), this high-energy emission should drive a photoevaporative wind. Indeed, the presence of such a wind has been inferred via analysis of mid-infrared [Ne II] emission from V4046 Sgr (Sacco et al. 2012). However, given the suite of models presented by Owen et al. (2011) and the present accretion rate of V4046 Sgr ( $\log \dot{M} = -9.3 \pm 0.3 \,\mathrm{M}_{\odot} \,\mathrm{yr}^{-1}$ ; Donati et al. 2011; Curran et al. 2011), the X-ray luminosity is too low to explain the large cavity size inferred here. However, X-ray photoevaporation (and perhaps even EUV/FUV photoevaporation) might find a natural role in explaining the depletion of material inside the innermost dust ring  $(r \lesssim 3 \text{ AU})$  inferred from the SED, see  $\S4.2.1$ ).

Perhaps the greatest mystery surrounding the V4046 Sgr disk is its existence: most theoretical and observational work suggests that disk dispersal processes should substantially diminish the observational signatures studied here well within the lifetime of this system and the few others like it (Clarke et al. 2001; Alexander et al. 2006b; Takeuchi et al. 2005; Currie et al. 2007, 2009). The modeling analysis conducted here unfortunately is unable to directly answer the question of why this gas-rich disk persists even at an age of 10-20 Myr. However, the inferred disk structure might be providing some clues. It might be possible that the cavity was formed early in the disk lifetime, stifling the viscous evolution process by severely limiting the gas accretion flow onto the central stars, and thereby slowing the natural evolution of the disk material. Alternatively, Alexander (2012) suggested that the tidal torque induced by a close binary on its disk may inhibit accretion and increase the lifetime of the circumbinary disk compared to that of a disk around a single star. Such scenarios are speculative: but it is interesting to note that most (if not all) of the known long-lived, gas-rich disks have evidence for low-density cavities at their centers.

Overall, the signatures of evolution in the transition disk hosted by V4046 Sgr are remarkable, suggesting that this target merits a focused effort moving forward with ALMA. Its close proximity and large physical size enables high resolution and high sensitivity observations. Furthermore, the stellar binarity aids the observations: it is too tight to affect the disk structure, but the high stellar mass means that the widths of gas disk emission lines is large and so spectral line observations can have good velocity resolution without sacrificing sensitivity. Observations are further aided by the

fact that it is an isolated system unaffected by cloud contamination. With all of this in mind, V4046 Sgr promises to be an excellent laboratory for studying disk evolution and planet formation: its old age means that evolutionary features are well-advanced, and its rich gas disk provides an excellent target for both detection efforts and spatially resolved analysis. Lastly, the X-ray luminosity makes V4046 Sgr a natural target for studying photoevaporation and its effects on disk evolution.

# 6. Summary

We have studied the structure of the V4046 Sgr circumbinary disk using high resolution, high sensitivity mm-wave observations from the SMA. By modeling the SED, spatially resolved 1.3 mm dust continuum, and line emission of three CO isotopes, we have identified this disk as an exemplar evolved protoplanetary disk. The key conclusions of our analysis are:

- 1. The CO gas disk is significantly more extended than the compact distribution of large grains. In order to reproduce this feature we decouple the dust and gas surface density profiles, reducing the dust-to-gas ratio in the outskirts of our disk model by a factor of 10. We interpret this phenomenon as the result of the simultaneous growth and inward radial drift of mm/cm-sized particles in a viscously evolving gas disk (Birnstiel et al. 2012a).
- 2. The V4046 Sgr disk features a large central cavity ( $r = 29 \,\mathrm{AU}$ ) depleted of mm/cm-sized dust grains. These grains are concentrated in a narrow ring ( $\mu = 37 \,\mathrm{AU}$ , FWHM=16 AU). There is no conclusive evidence from the CO line emission whether there is an analogous depletion in the gas disk. This distinctive morphology is consistent with simulations that feature large pressure traps generated by the dynamical interaction of a massive companion with a gas disk and the evolution of solid material (Pinilla et al. 2012a).
- 3. The cavity contains a significant population of  $\mu$ m-sized grains. We infer that this distribution of small dust particles has a smaller central clearing that may be consistent with X-ray photoevaporation (Owen et al. 2011), but is too large to be truncated by the central binary (Artymowicz & Lubow 1994). This population might originate from small grains entrained in the gas flowing past the pressure barrier that traps the mm/cm-sized grains in the large ring (Rice et al. 2006).

We are grateful to Adam Kraus for sharing his K-band limit on a companion, Andrea Isella for teaching K.R. about asymmetries, and Moritz Günther for helping us with the X-ray luminosities. We are also indebted to Kees Dullemond, Guillermo Torres, and Matt Payne for insightful discussions. We acknowledge support from NASA Origins of Solar Systems grant No. NNX11AK63. J.K.'s research on V4046 Sgr and other nearby protoplanetary disks is supported in part by National Science Foundation grant AST-1108950 to RIT. The Submillimeter Array is a joint project between

the Smithsonian Astrophysical Observatory and the Academia Sinica Institute of Astronomy and Astrophysics and is funded by the Smithsonian Institution and the Academia Sinica. This work is based [in part] on archival data obtained with the Spitzer Space Telescope, which is operated by the Jet Propulsion Laboratory, California Institute of Technology under a contract with NASA. Support for this work was provided by NASA.

Table 1. Summary of Observations

| UT date                                  | configuration                        | antennas    | baselines $[k\lambda]$ | $t_{\rm on}$ [min] | $\Delta \nu_{\rm cont}$ [GHz] | $	au_{ m atm} \ (225{ m GHz})$ |
|--|--------------------------------------|-------------|------------------------|--------------------|-------------------------------|--------------------------------|
| 2009 Feb 23<br>2009 Apr 25<br>2011 Mar 8 | extended<br>compact-N<br>sub-compact | 8<br>6<br>7 | 17-132<br>6-84<br>4-50 | 110<br>220<br>90   | 3.4<br>3.4<br>7.4             | 0.05<br>0.06<br>0.05           |
| $2011~{\rm Sep}~4$                       | very extended                        | 8           | 19-390                 | 180                | 7.4                           | 0.04                           |

### REFERENCES

Aikawa, Y., & Herbst, E. 1999, A&A, 351, 233

Alexander, R. D., Clarke, C. J., & Pringle, J. E. 2004, MNRAS, 354, 71

Alexander, R. D., Clarke, C. J., & Pringle, J. E. 2006, MNRAS, 369, 216

Alexander, R. D., Clarke, C. J., & Pringle, J. E. 2006, MNRAS, 369, 229

Alexander, R. D., & Armitage, P. J. 2007, MNRAS, 375, 500

Alexander, R. D., & Armitage, P. J. 2009, ApJ, 704, 989

Alexander, R. 2012, ApJ, 757, L29

Andrews, S. M., Wilner, D. J., Hughes, A. M., Qi, C., & Dullemond, C. P. 2009, ApJ, 700, 1502

Andrews, S. M., Wilner, D. J., Hughes, A. M., Qi, C., & Dullemond, C. P. 2010, ApJ, 723, 1241

Andrews, S. M., et al. 2011a, ApJ, 732, 42 (2011)

Andrews, S. M., Rosenfeld, K. A., Wilner, D. J., & Bremer, M. 2011b, ApJ, 742, L5 (2011)

Andrews, S. M., et al. 2012, ApJ, 744, 162

Argiroffi, C., Maggio, A., Montmerle, T., et al. 2012, ApJ, 752, 100

Artymowicz, P., & Lubow, S. H. 1994, ApJ, 421, 651

Baraffe, I., Chabrier, G., Allard, F., & Hauschildt, P. H. 1998, A&A, 337, 403

Barge, P., & Sommeria, J. 1995, A&A, 295, L1

Beichmann, C. A., Neugebauer, G., Habing, H. J., Clegg, P. E., & Chester, T. J. 1988, in Infrared Astronomical Satellie Catalogs and Atlases. Volume 1: Explanatory Supplement

Birnstiel, T., Dullemond, C. P., & Brauer, F. 2010, A&A, 513, A79

Birnstiel, T., Klahr, H., & Ercolano, B. 2012a, A&A, 539, 148 i

Birnstiel, T., Andrews, S. M., & Ercolano, B. 2012b, A&A, 544, A79

Birnstiel, T., Dullemond, C. P., & Pinilla, P. 2013, A&A, 550, L8

Brauer, F., Dullemond, C. P., & Henning, T. 2008, A&A, 480, 859

Brinch, C., & Hogerheijde, M. R. 2010, A&A, 523, 25

Brown, J. M., Blake, G. A., Qi, C., et al. 2009, ApJ, 704, 496

Brown, J. M., Rosenfeld, K. A., Andrews, S. M., Wilner, D. J., & van Dishoeck, E. F. 2012, ApJ, 758, L30

Byrne, P. B. 1986, Ir. Astron. J., 17, 294

Calvet, N., D'Alessio, P., Hartmann, L., Wilner, D., Walsh, A., & Sitko, M. 2002, ApJ, 568, 1008

Casassus, S., van der Plas, G., M, S. P., et al. 2013, Nature, 493, 191

Clarke, C. J., Gendrin, A., & Sotomayor, M. 2001, MNRAS, 328, 485

Crida, A., Morbidelli, A., & Masset, F. 2006, Icarus, 181, 587

Curran, R. L., Argiroffi, C., Sacco, G. G., et al. 2011, A&A, 526, A104

Currie, T., Balog, Z., Kenyon, S. J., et al. 2007, ApJ, 659, 599

Currie, T., Lada, C. J., Plavchan, P., et al. 2009, ApJ, 698, 1

D'Alessio, P., Calvet, N., & Hartmann, L. 2001, ApJ, 553, 321

Dartois, E., Dutrey, A., & Guilloteau, S. 2003, A&A, 399, 773

Dong, R., Rafikov, R., Zhu, Z., et al. 2012, ApJ, 750, 161

de la Reza, R., Quast, G., Torres, C. A. O., Mayor, M., Meylan, G., & Llorente de Andres, F. 1986, ESASP, 263, 107

Donati, J.-F., Gregory, S. G., Montmerle, T., et al. 2011, MNRAS, 417, 1747

Dutrey, A., Guilloteau, S., Piétu, V., et al. 2008, A&A, 490, L15

Goldreich, P., & Tremaine, S. 1980, ApJ, 241, 425

Gorti, U., & Hollenbach, D. 2009, ApJ, 690, 1539

Gorti, U., Dullemond, C. P., & Hollenbach, D. 2009, ApJ, 705, 1237

Guilloteau, S., Dutrey, A., Piétu, V., & Boehler, Y. 2011, A&A, 529, 105

Günther, H. M., Liefke, C., Schmitt, J. H. M. M., Robrade, J., & Ness, J.-U. 2006, A&A, 459, L29

Harris, R. J., Andrews, S. M., Wilner, D. J., & Kraus, A. L. 2012, ApJ, 751, 115

Hartmann, L., Calvet, N., Gullbring, E., & D'Alessio, P. 1998, ApJ, 495, 385

Henize, K. G. 1976, ApJS, 30, 491

Herbig, G. H., & Bell, K. R. 1988, Third Catalog of Emission-Line Stars of the Orion Population, Lick Observatory Bulletin #1111 (Santa Cruz, CA) Ho, P. T. P., Moran, J. M., & Lo, K. Y. 2004, ApJ, 616, L1

Hollenbach, D., Johnstone, D., Lizano, S., & Shu, F. 1994, ApJ, 428, 654

Hubickyj, O., Bodenheimer, P., & Lissauer, J. J. 2005, Icarus, 179, 415

Huenemoerder, D. P., Kastner, J. H., Testa, P., Schulz, N. S., & Weintraub, D. A. 2007, ApJ, 671, 592

Hutchinson, M. G., Evans, A., Winkler, H., & Spencer Jones, J. 1990, A&A, 234, 230

Isella, A., Carpenter, J. M., & Sargent, A. I. 2009, ApJ, 701, 260

Isella, A., Natta, A., Wilner, D., Carpenter, J. M., & Testi, L. 2010, ApJ, 725, 1735

Isella, A., Pérez, L. M., & Carpenter, J. M. 2012, ApJ, 747, 136

Jensen, E. L. N., Mathieu, R. D., & Fuller, G. A. 1996

Jensen, E. L. N., & Mathieu, R. D. 1997, AJ, 114, 301

Johansen, A., Youdin, A., & Klahr, H. 2009, ApJ, 697, 1269

Johnson, H. M. 1986, ApJ, 300, 401

Kastner, J. H., Zuckerman, B., Weintraub, D. A., & Forveille, T. 1997, Science, 277, 67

Kastner, J. H., Zuckerman, B., Hily-Blant, P., & Forveille, T. 2008, A&A, 492, 469

Kastner, J. H., Hily-Blant, P., Sacco, G. G., Forveille, T., & Zuckerman, B. 2010, ApJ, 723, L248

Kastner, J. H., Sacco, G. G., Montez, R., et al. 2011, ApJ, 740, L17

Klahr, H. H., & Henning, T. 1997, Icarus, 128, 213

Lejeune, T., Cuisinier, F., & Buser, R. 1997, A&AS, 125, 229

Lin, D. N. C., & Papaloizou, J. 1979, MNRAS, 188, 191

Lynden-Bell, D., & Pringle, J. E. 1974, MNRAS, 168, 603

Mayama, S., Hashimoto, J., Muto, T., et al. 2012, ApJ, 760, L26

Merrill, P. W., & Burwell, C. G. 1950, ApJ, 112, 72

Nataf, D. M., Stanek, K. Z., & Bakos, G. A. 2010, Acta Astronomica, 60, 261

Owen, J. E., Ercolano, B., Clarke, C. J., & Alexander, R. D. 2010, MNRAS, 401, 1415

Owen, J. E., Ercolano, B., & Clarke, C. J. 2011, MNRAS, 412, 13

Owen, J. E., Clarke, C. J., & Ercolano, B. 2012, MNRAS, 422, 1880

Öberg, K. I., et al. 2011, ApJ, 734, 98

Panić, O., Hogerheijde, M. R., Wilner, D., & Qi, C. 2008, A&A, 491, 219

Panić, O., Hogerheijde, M. R., Wilner, D., & Qi, C. 2009, A&A, 501, 269

Pérez, L. M., et al. 2012, ApJ, 760, L17

Pinilla, P., Benisty, M., & Birnstiel, T. 2012, A&A, 545, A81

Pinilla, P., Birnstiel, T., Ricci, L., et al. 2012b, A&A, 538, A114

Pollack, J. B., Hollenbach, D., Beckwith, S., Simonelli, D. P., Roush, T., & Fong, W. 1994, ApJ, 421, 615

Pollack, J. B., Hubickyj, O., Bodenheimer, P., Lissauer, J. J., Podolak, M., & Greenzweig, Y. 1996, Icarus, 124, 62

Qi, C., Wilner, D. J., Aikawa, Y., Blake, G. A., & Hogerheijde, M. R. 2008, ApJ, 681, 1396

Qi, C., et al. 2011, ApJ, 740, 84

Quast, G. R., Torres, C. A. O., de La Reza, R., da Silva, L., & Mayor, M. 2000, IAU Symposium, 200, 28P

Regály, Z., Juhász, A., Sándor, Z., & Dullemond, C. P. 2012, MNRAS, 419, 1701

Rice, W. K. M., Armitage, P. J., Wood, K., & Lodato, G. 2006, MNRAS, 373, 1619

Rodriguez, D. R., Kastner, J. H., Wilner, D., & Qi, C. 2010, ApJ, 720, 1684

Rosenfeld, K. A., Andrews, S. M., Wilner, D. J., & Stempels, H. C. 2012a, ApJ, 759, 119

Sacco, G. G., Flaccomio, E., Pascucci, I., et al. 2012, ApJ, 747, 142

Sacco. G. G., et al. 2013, in preparation

Schöier, F. L., van der Tak, F. F. S., van Dishoeck, E. F., & Black, J. H. 2005, A&A, 432, 369

Skrutskie, M. F., et al. 2006, AJ, 131, 1163

Stempels, H. C., & Gahm, G. F. 2004, A&A, 421, 1159

Stempels, H. C. 2013, in preparation

Takeuchi, T., & Lin, D. N. C. 2002, ApJ, 581, 1344

Takeuchi, T., Clarke, C. J., & Lin, D. N. C. 2005, ApJ, 627, 286

Tamura, M. 2009, American Institute of Physics Conference Series, 1158, 11

Torres, C. A. O., Quast, G. R., da Silva, L., de la Reza, R., Melo, C. H. F., & Sterzik, M. 2006, A&A, 460, 695

Torres, C. A. O., Quast, G. R., Melo, C. H. F., & Sterzik, M. F. 2008, Handbook of Star Forming Regions, Volume II, 757

van der Marel, N., van Dishoeck, E. F., Bruderer, S., et al. 2013, Science, 340, 1199

Weaver, W. B., & Jones, G. 1992, ApJS, 78, 239

Weidenschilling, S. J. 1977, MNRAS, 180, 57

Weidenschilling, S. J. 1980, Icarus, 44, 172

Weintraub, D. A. 1990, ApJS, 74, 575

Wilson, T. L. 1999, Reports on Progress in Physics, 62, 143

Zacharias, N., et al. 2010, AJ, 139, 2184

Zhu, Z., Nelson, R. P., Dong, R., Espaillat, C., & Hartmann, L. 2012, ApJ, 755, 6

This preprint was prepared with the AAS IATEX macros v5.2.